

GENERAL ATOMIC

DIVISION OF GENERAL DYNAMICS

GA-6882

(NASA-CR-74086) THE NEUTRON CAPTURE CROSS
SECTION OF THE TUNGSTEN ISOTOPES FROM 0.01
TO 10 ELECTRON VOLTS (General Dynamics
Corp.) 39 p

N76-70921

00/98 Unclas
29469

THE NEUTRON CAPTURE CROSS SECTION OF THE TUNGSTEN ISOTOPES FROM 0.01 TO 10 ELECTRON VOLTS

by

S. J. Friesenhahn, E. Haddad, F. H. Fröhner,
and W. M. Lopez

N67-87197

| | | |
|-------------------|--------------------------------|------------|
| FACILITY FORM 602 | X66-36243 N67-87197 | |
| | (ACCESSION NUMBER) | (THRU) |
| | 39 | 2A |
| | (PAGES) | (CODE) |
| | CR-74086 | 24 |
| | (NASA CR OR TMX OR AD NUMBER) | (CATEGORY) |

This work was supported in part by the National
Aeronautics and Space Administration, Space Nuclear
Propulsion Office, under Contract SNPC-27.

January 20, 1966

NOT FOR DISTRIBUTION
Only

GENERAL ATOMIC
DIVISION OF
GENERAL DYNAMICS

JOHN JAY HOPKINS LABORATORY FOR PURE AND APPLIED SCIENCE

P.O. BOX 608, SAN DIEGO, CALIFORNIA 92112

GA-6882

THE NEUTRON CAPTURE CROSS SECTION OF THE TUNGSTEN
ISOTOPES FROM 0.01 TO 10 ELECTRON VOLTS*

by

S. J. Friesenhahn, E. Haddad, F. H. Fröhner,
and W. M. Lopez

This is a preprint of a paper submitted for
publication in Nuclear Science and Engineering.

*This work was supported in part by the National
Aeronautics and Space Administration, Space Nuclear
Propulsion Office, under Contract SNPC-27.

January 20, 1966

[REDACTED]

[REDACTED]

ABSTRACT

Capture cross section measurements from 0.01 to 10 eV on W^{182} , W^{183} , W^{184} , and W^{186} employing a totally absorbing gamma-ray detector are described. The 2200 m/sec value of the capture cross section is compared with previously reported measurements, and the shape and magnitude of the cross section curve are compared with calculations using reported resonance parameters. Parameters of negative energy levels required to account for the discrepancy between measured and calculated cross sections for W^{182} and W^{184} are given. A measurement of the gold capture cross section is used as a check on the techniques employed.

CONTENTS

| | |
|--|----|
| INTRODUCTION | 1 |
| EXPERIMENTAL TECHNIQUES | 2 |
| Apparatus | 2 |
| Detector | 3 |
| Flux Measurement | 4 |
| Gold Cross Section | 7 |
| Samples Used | 7 |
| CROSS SECTION ANALYSIS | 8 |
| EXPERIMENTAL RESULTS | 11 |
| ERRORS | 13 |
| CONCLUSIONS | 13 |
| ACKNOWLEDGMENTS | 14 |
| Appendix--MULTIPLE SCATTERING CORRECTION | 15 |
| REFERENCES | 18 |
| FOOTNOTES | 20 |
| TABLES | 21 |
| FIGURES | 25 |

INTRODUCTION

The use of tungsten as a structural material for high-temperature reactors has become of interest because of the very high melting point of tungsten. Since the thermal neutron capture cross section of tungsten is not small it is important to have accurate capture cross sections in the region of the Maxwellian neutron velocity distribution. Because of the large temperature difference between startup and operation, the energy dependence of the capture cross section must be known over an appreciable energy interval. The capture cross section shape may deviate from a $1/v$ dependence due to both positive and negative energy levels near the neutron binding energy of the compound nucleus, and hence knowledge of the 2200 m/sec value is not sufficient.

Several techniques have been employed to obtain capture cross sections in the low-energy region:

1. Pile oscillator technique: (1) This method requires that the cross section have a $1/v$ dependence, or a known energy dependence with which the value obtained can be corrected.
2. Activation measurements: (2) This technique can be employed to obtain capture cross sections if the decay scheme of the product nucleus is known and if states with suitable half-lives are present.
3. Total cross section measurements: Information about the capture cross section can be obtained from this kind of measurement provided the scattering cross section is either small or well known, neither of which is the case for tungsten. Complications arise with this method due to the crystalline binding effects, and hence it is usually the practice to measure the total cross section

at energies below the Bragg cutoff and to extrapolate to thermal energies assuming a $1/v$ cross section dependence. (3) A correction must still be made, however, for incoherent scattering. (4)

4. Calculations using resonance parameters: The low-energy cross section can be calculated from measured resonance parameters; however, resonance parameter determinations are subject to analytical and experimental limitations that usually result in undesirably large errors. The calculations are further hampered by the lack of information on resonances outside the measured region, particularly negative energy levels.

Obviously a direct energy-dependent measurement of the capture cross section is desirable. To our knowledge no such measurement on any isotope has been reported in the literature. In this paper we shall describe the capture cross section measurements on the four most abundant tungsten isotopes, W^{182} , W^{183} , W^{184} , and W^{186} . No attempt will be made to obtain the cross sections in the peak regions of the low-energy resonances, where the multiple scattering effects are large and are strongly dependent on resonance parameters.

EXPERIMENTAL TECHNIQUES

APPARATUS

The neutron source used in these measurements was the General Atomic linear accelerator. The machine parameters used were: electron energy, 28 MeV; currents, 0.3 to 1 A; and burst widths, 0.05 to 4.5 μ sec at 22.5 pulses/sec. The shorter burst widths were used to reduce the counting rate for the high cross section sample runs and to obtain high-resolution flux-calibration data. The electron target assembly is shown in Fig. 1. The electrons slowing down in the Fansteel¹ target produced bremsstrahlung, which in turn produced high-energy neutrons with a broad maximum near 1 MeV. These neutrons were slowed down to the epithermal

and thermal region by the water container, which also acted as a coolant for the target.

The neutron energy was determined by conventional time-of-flight techniques. The effective flight-path length was 18.61 ± 0.01 meters, which includes a 0.03 meter correction for neutron slowing-down time and the neutron scattering mean free path in the moderator. The entire flight path was maintained at a pressure of less than 150 microns Hg, including an additional 2.5 meters beyond the sample. The electronics used for the time-of-flight and pulse-height data acquisition are shown in Fig. 2. Not shown are the two independent BF_3 flux-monitoring channels, which sample the penumbra of the beam just before it enters the scintillator. The sum of the counts in the two monitors was taken to be proportional to the neutron flux at the sample. The signals from the monitors are turned off for $50 \mu\text{sec}$ following the accelerator burst to eliminate effects due to accelerator noise pickup and bremsstrahlung.

DETECTOR

In the work reported here, the capture cross section was measured by observing the prompt gamma rays that are emitted by the compound nucleus upon neutron capture. In general, several gamma rays are emitted whose spectral distribution is a function of the capturing isotope and the neutron energy. The total energy of the gamma rays is very nearly equal to the neutron binding energy of the compound nucleus. The difference between the prompt gamma-ray energy and the neutron binding energy is due to the kinetic energy of the capturing neutron, which is very small at the neutron energies considered here, and may also be due to long-lived product nucleus activity. Since it is usually not possible to make corrections for changes in gamma spectra with neutron energy, it is important that the gamma-ray detector have a gamma-detection efficiency that is independent of the gamma spectrum. This has been achieved by the high-efficiency large liquid scintillator that was used for these measurements. (Details of the detector may be found in Ref. 5.) Briefly, the detector (see Fig. 3) consists of a

2-ft. diam., hollow central Plexiglas annulus surrounded by an array of forty-four 9-in. diam., hollow Plexiglas cylinders (logs). Each end of an individual log is viewed by a 5-in. photomultiplier tube (CBS-7819 or Dumont 6364). To reduce light losses, the areas at the ends of each log not covered by the photomultiplier were painted with white Tygon paint. Each end of the central annulus is viewed by eight 5-in. photomultiplier tubes. The samples for the tungsten measurements were placed in an evacuated 6.0-in. -diam. aluminum liner positioned inside and concentric to a 6.5-in. -diam. hole that extends through the central annulus. Wrapped around the aluminum liner was a 0.125-in. -thick B¹⁰ epoxy sheet. The collimated neutron beam enters the detector through a 0.020-in. aluminum window, then passes into the evacuated liner. The liquid scintillator solution used in the logs is decahydronaphthalene (decalin) containing 1 g/liter of p-terphenyl, 2 g/liter of 2,5 diphenyloxazole (PPO), and 0.05 g/liter of dimethyl-p-bis[2-(5-phenyloxizoyl)]-benzene (dimethyl-POPOP). The scintillator solution used in the 2-ft. central annulus was the same as that used in the logs with one exception: it also contained trimethyl-borate (10% by volume). The trimethyl-borate was added to the solution in the central annulus to suppress the 2.2-MeV gamma rays resulting from in-scattered neutrons being captured by hydrogen.

FLUX MEASUREMENT

The problem of determining the instantaneous absolute neutron flux at the sample can be divided into two parts: (1) the determination of the shape of the $\phi(t)$ versus t curve, and (2) the normalization of this curve to make it absolute.

The flux-shape determination is most easily accomplished by observing the capture gamma rays from a sample positioned inside the scintillator which captures essentially all of the incident neutrons. This allows the flux-shape determination to be made using the same flight path and detector as employed in the capture data runs.

The thickness of the material that can be used is limited by the self-absorption of capture gamma rays in the sample. If this absorption becomes large, the fraction of the gamma rays escaping may become a function of the neutron capture cross section of the sample. This arises from the fact that a capture event occurring near the front face (which is more likely when the cross section is relatively high) can have an appreciably higher probability of being detected than one that originates in the interior due to the exponential nature of the gamma attenuation. The three materials investigated for this purpose were:

| <u>Material</u> | <u>Thickness (g/cm²)</u> | Useful |
|--------------------|-------------------------------------|--------------------------|
| | | <u>Energy Range (eV)</u> |
| boron ² | 0.804 | 0.01 - 1.2 |
| cadmium | 0.677 | 0.01 - 0.28 |
| indium | 12.94 | 0.01 - 2.0 |

The indium sample was found to show an appreciable neutron energy-dependent gamma-ray self-absorption effect and hence was not used. For the boron sample, the calculated effect of self-absorption of gamma-rays on the flux shape was much less than 5%, and hence no correction was made. The gamma-ray absorption was completely negligible in the case of cadmium. A comparison between the cadmium and boron flux shapes yielded excellent agreement between 0.01 and 0.28 eV, and above this energy the boron flux shape was checked against a thin BF₃ counter. The comparisons are shown in Fig. 4 in which it can be seen that the shapes agree within the statistical accuracy of the points, i. e., <1%.

From 1 to 10 eV the flux shape was measured with a 2-in. -diam. 1 atmosphere BF₃ counter. After a 3% self-protection correction was applied to the data, the flux shape could be fitted within the statistical accuracy of the data to an exponential of the form $\phi(t) = KE^\alpha$, where K is a constant to be determined, E is the energy in eV, and α is the slope of the log $\phi(t)$ versus log E plot. For the target assembly used, $\alpha = 0.531 \pm 0.005$.

This exponential fit to the flux shape was made absolute by the saturated resonance technique. This consists of measuring the counting rate in an energy region in which essentially all of the incident neutrons are captured. For reasons to be discussed later, the most convenient material to use is the material whose cross section is to be measured. It is important that capture predominate over scattering in order to reduce the corrections for scattered neutrons lost from the sample, and the thickness of the material must not be sufficient to produce appreciable gamma absorption effects. These two conditions are fulfilled only in the 4.15-eV resonance in W^{182} and the 4.906-eV resonance in gold. Typical flux-calibration data are shown in Fig. 5. The region of negligible transmission is indicated by the flattening of the resonance peak. The energy interval indicated in Fig. 5 was chosen for the flux normalization, and the data were corrected for resolution and multiple scattering effects (6) using the resonance parameters obtained by Bernabei (7) in the case of W^{182} , and the BNL-325 (8) parameters for gold. In both cases the corrections for resolution and scattering were small (<3%) and hence the errors in the normalizations due to errors in the resonance parameters are negligible.

Having obtained the absolute counting rate at the energy of the calibrating resonance, we have

$$K = \frac{c(\tau_0)}{\epsilon_i S E_0^\alpha}$$

where ϵ_i = the efficiency for the detection of a capture event,

$c(\tau_0)$ = the counting rate observed at the time corresponding to the resonance energy (counts/cm²/monitor count),

S = the area of the calibrating sample (cm²), and

E_0 = the resonance energy (eV).

The 0.01- to 1.2-eV flux shape was normalized to the absolute exponential flux in the 1.05- to 1.2-eV region. The absolute flux shape expressed in terms of accelerator parameters is shown in Fig. 6.

Gold Cross Section

An excellent check on the flux measurements just described is a comparison of the gold capture cross section obtained using this flux with the best available gold capture cross sections obtained by the indirect techniques mentioned in the introduction. A compilation of the gold capture cross sections obtained by these techniques has recently been made (9) and points generated from a fit to data points listed in the compilation are shown in Fig. 7, in which $\sigma_{\gamma} \sqrt{E}$ has been plotted to allow an expanded scale at low energies. Also shown in this figure is the capture cross section calculated using the high and low values for the $\Gamma_{\gamma} \Gamma_n$ product quoted in BNL-325 (8) for the 4.906-eV level and the best values for the higher energy resonances up to 1 keV as measured at Saclay, (10) including a statistical correction for resonances above 1 keV. The BNL-325 recommended value for the 2200 m/sec cross section is also indicated. The experimental data points obtained in this work were not normalized in any way and hence represent an absolute determination of the cross section throughout the energy range. As can be seen from the figure, the agreement is quite good. Figure 8 shows a comparison of the measured gold capture cross section with the curve calculated from the best values of the 4.906-eV parameters and the best Saclay parameters for the higher energy resonances. These comparisons lend support to the conclusion that the flux-measurement techniques just described yield results that are probably reliable to $\pm 1\%$ in the 0.01- to 10-eV energy region.

Samples Used

The gold and natural tungsten data were taken using high-purity metallic disks 2 inches in diameter. The sample thicknesses were 7.294×10^{-4} and 1.795×10^{-3} atoms/barn, respectively. The tungsten isotopic cross section data were acquired using tungsten trioxide powder with the thicknesses and enrichments listed in Table 1.

The tungsten trioxide powder was pressed into thin-wall aluminum canisters under approximately 1000 kg/cm^2 pressure. Radiographs indicated that the samples prepared in this fashion were uniform to better than $\pm 5\%$ in thickness. The weights of the canisters were all adjusted to 10 grams, and an empty canister was placed in the detector to measure the correction to be applied to the tungsten data for captures in the canister material. This correction was increased to account for the increased capture rate in the canister material due to multiple scattering from the tungsten trioxide powder.

CROSS SECTION ANALYSIS

The counts observed in a time channel due to captures in isotope i can be written

$$c_i(\tau) = \epsilon_i S \phi(\tau) (1 - e^{-N\sigma}) \frac{a_i \sigma_{\gamma i} f}{\sigma f_0}, \quad (1)$$

where ϵ_i = fraction of the capture events observed in the pulse-height window (usually 4 to 10 MeV),

$\phi(\tau)$ = neutron flux (neutrons/cm²/monitor count),

N = number of sample atoms/cm²,

σ = total cross section (scattering plus capture),

a_i = abundance of the i^{th} isotope,

$\sigma_{\gamma i}$ = capture cross section of the i^{th} isotope,

S = sample area (cm²),

f_0 = probability of capture of an incident neutron on the first interaction, and

f = total neutron capture probability.

The ratio f/f_0 describes the multiple scattering effect, which will be discussed later.

In the case of tungsten, more than one isotope contributes to the observed capture rate due to the finite enrichment; hence,

$$c(\tau) = \sum_i c_i(\tau), \quad (2)$$

where the summation is taken over all the isotopes present (= 4 in the present case).

Solving Eq. (2) for the capture cross section of the i^{th} isotope we obtain

$$\sigma_{\gamma i} = \left[\frac{c(\tau)\sigma f_0}{S\phi(\tau)(1 - e^{-N\sigma})f} - \sum_{k \neq i} a_k \epsilon_k \sigma_{\gamma k} \right] (a_i \epsilon_i)^{-1}. \quad (3)$$

The summation in Eq. (3) is taken over the depleted isotopes. In the case of natural tungsten (or gold), where the sum of the abundance-weighted isotopic capture cross sections is being measured, Eq. (3) becomes

$$\sigma_{\gamma t} = \frac{c(\tau)\sigma f_0}{\epsilon_t S\phi(\tau)(1 - e^{-N\sigma})f}, \quad (4)$$

where ϵ_t is the fraction of the natural sample captures detected in the bias interval and is calculated from

$$\epsilon_t = \frac{\sum_i \epsilon_i a_i \sigma_{\gamma i}}{\sum_i a_i \sigma_{\gamma i}}.$$

Equations (3) and (4) must be solved by iteration since σ , f_0/f , $\sum a_k \epsilon_k \sigma_{\gamma k}$, and ϵ_t are all functions of the capture cross sections being measured. A computer code was written which performs the required iteration and obtains the best values of the isotopic and natural cross sections.

In order to determine ϵ_i , time-gated pulse-height distributions were taken for captures in the lowest energy strong resonance in each of the isotopes. In order to minimize errors due to background subtractions, the

"sliding window" method of background accumulation was employed. In this technique the sample is left in position and the time window is moved to flight times slightly earlier and then slightly later than the time corresponding to the resonance in question. Since the time-dependent backgrounds vary only slightly within the width of a typical resonance, the average background accumulated in this fashion is representative of the background in the resonance itself. Using this technique the pulse-height data were reliable down to ≈ 1.5 MeV. Below this energy an extrapolation to zero bias is necessary. As can be seen from the measured pulse-height distributions shown in Figs. 9 and 10, a linear extrapolation is consistent with the shape of the distributions. The area under the curves below 1.5 MeV is about 4% of the total. It is highly improbable that the extrapolation could be in error by more than $\pm 50\%$, and hence a $\pm 2\%$ error in the bias efficiency was assumed.

The solution of Eqs. (3) and (4) requires a knowledge of the multiple scattering effect, i.e., f_0/f . The multiple scattering correction employed (see Appendix) is a first order analytic calculation of the fraction f_1 of neutrons which are captured after the first scattering collision. The scattering cross sections for tungsten were those calculated from the resonance parameters listed in Ref. 11.³ The low-energy scattering cross sections listed in Ref. 9 were used for oxygen and aluminum, and the potential scattering cross section as determined by Seth (12) was used for gold.⁴

The calculation ignores energy changes of the scattered neutron and the effects of thermal motion of the scattering nucleus. These effects are appreciable in the peak region of the low-energy resonances and hence no attempt was made to analyze the data in these regions.

The sample was considered to be an infinite slab, which is justified by the large diameter-to-thickness ratios for the samples employed. The geometric series approximation $f_0/f = 1 - f_1/f_0$ was used as the correction for the total of all scattered neutron captures.

In all cases the multiple scattering correction applied was less than 15%.

EXPERIMENTAL RESULTS

The values obtained in this work for the thermal cross section of W^{182} , W^{183} , W^{184} , and W^{186} are given in Table II. Also included are the values recommended in BNL-325 and the values calculated from the measured resonance parameters of the positive energy states.

The natural tungsten cross sections listed in Table II were obtained using the abundances as measured by White. (15) The relative contributions of the various isotopes to the natural tungsten thermal cross section can be seen in Table III.

The energy dependence of the cross sections is shown in Figs. 11 through 15. The time-of-flight data, after being corrected for analyzer dead time and backgrounds, were grouped and interpolated on a set of energy points. These energy points correspond to the data points shown in the figures. In all cases the neutron energy resolution width is much smaller than the energy difference between the points shown. Data points in the vicinity of the low-energy resonances are unreliable due to the effects of multiple scattering and resolution, and hence these points are not shown in the figures.

The measured W^{182} cross section shown in Fig. 11 is significantly higher than that calculated from positive energy resonances including a statistical term for the unresolved region. The discrepancy can be accounted for by postulating a $1/v$ contribution from negative energy levels. The choice of parameters for such a level is arbitrary, with the sole restriction that the "resonance" energy be much less than -10 eV in order that its contribution vary essentially as $1/v$ in the region of the measurement. Since W^{182} is an even-even nucleus, $g = 1$. The best choice of Γ_γ is the average radiation width of the positive energy levels, i.e., 57 meV. The

average reduced neutron width of $20 \text{ meV/eV}^{1/2}$ was chosen, which yields a resonance energy of -30.7 eV , and this is sufficiently small to yield a $1/v$ contribution. The dashed curve shown in Fig. 11 was obtained by adding this contribution to that of the positive energy levels. There is some indication that the negative energy contribution does not quite vary as $1/v$ because of the systematic deviation near 10 eV . No attempt was made to improve the fit by the inclusion of a non- $1/v$ negative energy contribution, due to the doubtful significance of the deviation.

The W^{183} cross section shown in Fig. 12 is slightly below the calculated curve by an amount which exceeds the errors in this measurement. The discrepancy is thought to be due to errors in the resonance parameters used.

The W^{184} data points shown in Fig. 13 lie well above the calculated curve, which again indicates a negative energy contribution. The "parameters" for the negative energy level obtained in the same fashion as those for W^{182} are: $g = 1$, $\Gamma_\gamma = 57 \text{ meV}$, $\Gamma_n^0 = 48.4 \text{ meV}$, and $E_0 = -110 \text{ eV}$. Again there is an indication of a non- $1/v$ negative energy contribution, and the significance of this deviation is again doubtful.

Three calculated cross section curves for W^{186} are shown in Fig. 14. The upper one was obtained from the parameters listed in Ref. 11 and the lower one from those listed in Ref. 16. It can be seen that the data points lie at an intermediate position. Since the cross section is dominated by the 18.8-eV level, the error can probably be ascribed to the $\Gamma_n\Gamma_\gamma$ product for this level, which is $1.413 \times 10^{-2} \text{ eV}^2$ for the measured curve as opposed to $1.648 \times 10^{-2} \text{ eV}^2$ for the upper calculated curve and $1.197 \times 10^{-2} \text{ eV}^2$ for the lower one. The radiation width was arbitrarily adjusted to force agreement at thermal energy. The result is the solid curve, which is in good agreement with the data throughout the measured energy interval.

The measured cross section of natural tungsten is shown in Fig. 15 along with a calculation from the positive energy parameters listed in Ref. 11. Also shown is the calculated cross section, including the two

negative energy levels evaluated earlier as well as the adjusted radiation width of the 18.8-eV level in W^{186} . These two curves agree below 1 eV because of a fortuitous cancellation of the errors in the isotopic cross sections calculated from the positive energy parameters. The natural tungsten cross section obtained by abundance-weighting the measured isotopic cross sections is also shown. The cross section of natural tungsten obtained in this way is in very good agreement with the measured cross section of natural tungsten except in the region near 10 eV where statistical uncertainties are appreciable.

ERRORS

The error sources involved in the cross section determination fall into three classes: (1) errors that affect the normalization, (2) errors that affect the energy scale, and (3) errors that affect the shape of the curve relative to the normalization point. Some of the errors involved are not analytic in nature, and hence only subjective estimates can be given. Table IV enumerates all known sources of errors and their estimated magnitude for each of the isotopes.

CONCLUSIONS

The magnitudes of the 2200 m/sec cross sections for W^{182} , W^{183} , W^{184} , and W^{186} have been obtained with appreciably smaller errors than have been previously reported. The capture cross section shapes reported here for the tungsten isotopes are the first in this energy region, and illustrate the utility of the technique as a check on measured low-energy resonance parameters and in the determination of negative energy level effects. The agreement between the cross section of natural tungsten as measured directly with that obtained from isotopic cross sections, as well as the agreement of the gold cross section with the best values available,

lend support to the belief that the techniques used here will be of value in obtaining accurate low-energy capture cross sections for most of the isotopes of interest in reactor physics.

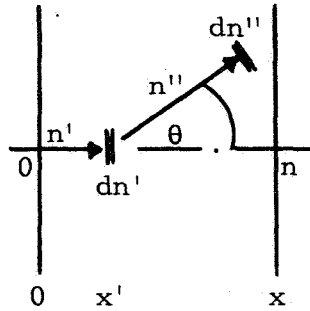
ACKNOWLEDGMENTS

We would like to acknowledge the assistance of J. R. Beyster, J. C. Young, and J. Neill in the low-energy flux shape measurements, and of F. Bell in apparatus fabrication.

Appendix

MULTIPLE SCATTERING CORRECTION

Consider the case of capture after zero or 1 scattering collision, for which the probabilities are f_0 and f_1 .



Probability that the neutron travels a distance x' :

$$e^{-Nx'\sigma} = e^{-n'\sigma} \quad (\sigma = \text{total cross section}).$$

Probability that it is scattered in a layer dn' :

$$dn'\sigma_n \quad (\sigma_n = \text{scattering cross section}).$$

Probability that the center of mass system scattering angle is θ_0 :

$$d(\cos \theta_0)/2 = d\mu_0/2 \quad (\text{isotropic scattering}).$$

Probability that the laboratory scattering angle is θ :

$$(d\mu/2)(d\mu_0/d\mu) \quad (\mu = \cos \theta).$$

Probability that the neutron travels a distance x'' :

$$e^{-Nx''\sigma'} = e^{-n''\sigma'}.$$

Probability that it is captured within dn'' :

$$dn''\sigma'_\gamma \quad (\sigma' \text{ and } \sigma'_\gamma \text{ are the cross sections after the first collision}).$$

The total probabilities for the combined events and for all possible combinations of n' , θ , and n'' are

$$f_0 = \int_0^n e^{-n'\sigma} dn'\sigma_\gamma = (1 - e^{-n\sigma}) \frac{\sigma_\gamma}{\sigma} \quad (1)$$

and

$$f_1 = \int_0^n e^{-n'\sigma} dn'\sigma_n \left[\int_{-1}^0 \frac{d\mu}{2} \frac{d\mu_0}{d\mu} \int_0^{-n'/\mu} e^{-n''\sigma'} dn''\sigma'_\gamma + \int_0^1 \frac{d\mu}{2} \frac{d\mu_0}{d\mu} \int_0^{(n-n')/\mu} e^{-n''\sigma'} dn''\sigma'_\gamma \right]. \quad (2)$$

For thermal neutrons the average energy loss in the scattering collision is zero; thus, we can put $\sigma' \approx$ and $\sigma'_\gamma \approx \sigma_\gamma$. Since $1/v$ cross sections are not affected by Doppler broadening, we can also use the stationary target approximation. The latter yields

$$\frac{d\mu_0}{d\mu} = \frac{\left[\mu + (A^2 - 1 + \mu^2)^{\frac{1}{2}} \right]^2}{A(A^2 - 1 + \mu^2)^{\frac{1}{2}}}. \quad (3)$$

For $A = \infty$, $d\mu_0/d\mu = 1$, and in this special case we can carry out the integrations in Eq. (2). We define $F_1(\infty, s)$ by

$$f_1 \equiv \frac{\sigma_n \sigma_\gamma}{\sigma^2} F_1(\infty, s),$$

where $s = N\sigma$. Then the integrations yield

$$F_1(\infty, s) = \frac{1}{2} \left\{ (1 - e^{-s})^2 - (1 - e^{-s}) s \operatorname{Ei}(-s) + (1 + e^{-s}) [\operatorname{Ei}(-s) - \ln Cs] - \operatorname{Ei}(-2s) + \ln 2Cs \right\}$$

$$\approx \frac{s^2}{2} \left[-\ln Cs \left(1 - \frac{s}{2} \dots \right) + \frac{3}{2} - \frac{5}{15} s \dots \right],$$

where

$$\operatorname{Ei}(-s) = \int_{-\infty}^s \frac{e^x}{x} dx = \ln Cs - \frac{s}{1 \cdot 1!} + \frac{s^2}{2 \cdot 2!} - \dots,$$

$$\ln Cs = \ln C + \ln s = 0.57722 \dots + \ln s,$$

$$f_0 = (1 - e^{-s})^{\frac{\sigma}{\gamma}}.$$

The geometric series approximation

$$f = f_0 + f_1 + f_2 + \dots \approx f_0 \left[1 + \frac{f_1}{f_0} + \left(\frac{f_1}{f_0} \right)^2 + \dots \right]$$

yields

$$f \approx \frac{f_0}{1 - (f_1/f_0)}$$

or

$$\frac{f_0}{f} = 1 - \frac{f_1}{f_0} = 1 - \frac{\sigma_n s^2}{2\sigma(1 - e^{-s})} \left[-(0.57722 \dots + \ln s) \left(1 - \frac{s}{2} \right) + \frac{3}{2} - \frac{5}{12} s \dots \right].$$

REFERENCES

1. D. J. Hughes, Pile Neutron Research, Addison-Wesley Publishing Co., Cambridge, Massachusetts, 1953.
2. W. S. Lyon, Nucl. Sci. Eng. 8, 378-380 (1960).
3. R. E. Schmunk, P. D. Randolph, and R. M. Brugger, Nucl. Sci. Eng. 7, 193-197 (1960).
4. R. S. Carter, H. Palevsky, V. W. Myers, and D. J. Hughes, Phys. Rev. 92, 716-721 (1953).
5. E. Haddad, R. B. Walton, S. J. Friesenhahn, and W. M. Lopez, Nucl. Instr. Methods 31, 125-138 (1964).
6. F. H. Fröhner and E. Haddad, Nucl. Phys. 71, 129-156 (1965).
7. Austin Bernabei, "The Effects of Crystalline Binding on the Doppler Broadening of a Neutron Resonance," USAEC Report BNL-860, Brookhaven National Laboratory, April 1, 1964.
8. D. J. Hughes and R. B. Schwartz, "Neutron Cross Sections," USAEC Report BNL-325, 2nd ed., Brookhaven National Laboratory, July 1, 1958.
9. R. C. Barrall and W. M. McElroy, "Neutron Flux Spectra Determination by Foil Activation," AFWL-TR-65-34, Vol. II, August 1965.
10. J. Julien, et al., "Détermination du Spin et des Paramètres des Résonances pour $^{197}\text{Au} + n$ de 10 eV à 1000 eV" (to be published).
11. G. D. Joanou and C. A. Stevens, "Neutron Cross Sections for Tungsten Isotopes," NASA-CR-54261 (GA-5885), General Atomic Division, General Dynamics Corporation, November 13, 1964.
12. K. K. Seth, D. J. Hughes, R. L. Zimmerman, and R. C. Garth, Phys. Rev. 110, 692-700 (1958).

13. J. E. Russell, R. W. Hockenbury, and R. C. Block, "Neutron Capture Measurements on the Isotopes of Tungsten," in "Reports to the AEC Nuclear Cross Sections Advisory Group, Meeting at E. I. DuPont de Nemours and Company Savannah River Laboratory, January 28-30, 1964," WASH-1046, p. 104.
14. D. Shook and D. Bogart, Trans. Am. Nucl. Soc. 8, 284-285 (1965).
15. J. R. White and A. E. Cameron, Phys. Rev. 74, 991-1000 (1948).
16. D. J. Hughes, B. A. Magurno, and M. K. Brussel, "Neutron Cross Sections," USAEC Report BNL-325, 2nd ed., Suppl. 1, Brookhaven National Laboratory, January 1, 1960.

FOOTNOTES

1. 85% tungsten, 7.5% copper, and 7.5% nickel alloy manufactured by Fansteel Corporation.
2. In this measurement advantage was taken of the modular construction of the scintillator by turning off all but the central cylinder, thus allowing the 470-keV boron capture gamma rays to be observed under low background conditions.
3. The low-energy scattering cross sections listed in Ref. 11 seem to be in error.
4. These scattering cross sections were also used in the calculation of the total cross sections.

TABLE I
Abundances and Thicknesses of Enriched Tungsten Samples

| Enriched Isotope | Abundances | | | | | Thickness (atoms/barn) |
|------------------|------------|--------|--------|--------|--------|------------------------|
| | 180 | 182 | 183 | 184 | 186 | |
| 182 | <0.0003 | 0.945 | 0.0209 | 0.0234 | 0.0109 | 2.423×10^{-3} |
| 183 | <0.001 | 0.052 | 0.813 | 0.073 | 0.062 | 8.685×10^{-4} |
| 184 | <0.0005 | 0.0174 | 0.0174 | 0.942 | 0.0235 | 2.452×10^{-3} |
| 186 | <0.001 | 0.0057 | 0.0041 | 0.0183 | 0.972 | 1.270×10^{-3} |

TABLE II
Capture Cross Section at 0.0253 eV

| Isotope | BNL-325 | From Parameters | This Work |
|-------------------------|-----------|--------------------|-----------|
| 180 | 60.0±60.0 | a | ---- |
| 182 | 20.0±2.0 | 13.5 | 20.7±0.5 |
| 183 | 11.0±1.0 | 9.5 | 10.0±0.3 |
| 184 | 2.0±0.3 | 0.76 | 1.7±0.1 |
| 186 | 35.0±3.0 | 44.2 ^b | 37.8±1.2 |
| Natural | 19.2±1.0 | 19.9 | 18.3±0.5 |
| Calculated ^c | 17.5 | 18.2 | 18.3±0.5 |
| Gold | 98.8±0.3 | 97.0 | 98.7±1.8 |

^aThere are no reported parameters for W¹⁸⁰; however, a resonance at 15.8 eV has been assigned to this isotope (13).

^bA recent infinite dilution resonance integral measurement on W¹⁸⁶ (14) yielded a value 20% lower than that calculated from resonance parameters, which may indicate that the reported radiation width of the 18-eV level is too large.

^cCalculated abundance-weighted cross section using 60 barns for W¹⁸⁰. The agreement between the measured and calculated natural cross section of this work is fortuitous.

TABLE III

Contributions of Isotopes to Thermal Cross Section of Natural Tungsten

| Isotope | Natural Abundance | Thermal Capture Cross Section (barns) | Thermal Contribution (barns) | % of Total |
|---------|-------------------|---------------------------------------|------------------------------|----------------|
| 180 | 0.00126 | $(60.0 \pm 60.0)^a$ | 0.076 ± 0.076 | 0.4 ± 0.4 |
| 182 | 0.2631 | 20.7 ± 0.5 | 5.45 ± 0.13 | 29.8 ± 0.7 |
| 183 | 0.1428 | 10.0 ± 0.3 | 1.42 ± 0.04 | 7.8 ± 0.2 |
| 184 | 0.3064 | 1.7 ± 0.1 | 0.52 ± 0.03 | 2.8 ± 0.2 |
| 186 | 0.2864 | 37.8 ± 1.2 | 10.83 ± 0.34 | 59.2 ± 1.9 |

^aBNL-325 value used.

TABLE IV
Error Sources and Estimated Magnitude

| Error Type | % Error | | | | |
|---|-------------------|-------------------|------------------|------------------|-------------------|
| | W ¹⁸² | W ¹⁸³ | W ¹⁸⁴ | W ¹⁸⁶ | Au ¹⁹⁷ |
| Class (1), Errors in Normalization | | | | | |
| 1-1 Parameters of flux calibration resonances (4.15 eV in W ¹⁸² and 4.906 eV in Au ¹⁹⁷) | _____ | _____ | <0.01 | _____ | <0.01 |
| 1-2 Resolution correction to flux calibration | _____ | _____ | 0.04 | _____ | <0.01 |
| 1-3 Analyzer dead time correction | _____ | _____ | <0.01 | _____ | <0.01 |
| 1-4 Statistical errors in calibration interval | _____ | _____ | 0.7 | _____ | 0.6 |
| 1-5 Background subtraction in calibration | _____ | _____ | <0.01 | _____ | <0.01 |
| 1-6 Purity and deviation from stoichiometric composition | _____ | _____ | 1.0 | _____ | 0.1 |
| 1-7 Extrapolation to zero bias | _____ | _____ | 2.0 ^a | _____ | 0 |
| 1-8 Gain shift after normalization | _____ | _____ | 0.8 | _____ | 0.7 |
| 1-9 Gamma attenuation in sample | _____ | _____ | 0-1 | _____ | 0 |
| 1-10 Error in flux shape exponent | _____ | _____ | 0.9 | _____ | 1.7 |
| Class (2), Errors in Energy Scale | | | | | |
| 2-1 Flight path length | _____ | _____ | 0.1 | _____ | _____ |
| 2-2 Frequency or analyzer clock | _____ | _____ | 0.2 | _____ | _____ |
| 2-3 Analyzer start time | _____ | _____ | 1.0-0.02 | _____ | _____ |
| Class (3), Shape Errors | | | | | |
| 3-1 Scattering cross section used in multiple scattering calculation | 0.5 | 0.3 | 0.8 | 0.3 | 0.02 |
| 3-2 Assumption of no energy change in scattered neutrons, infinite slab approximation and isotropic scattering approximation in multiple scattering calculation | <0.1 ^b | <0.1 ^b | <0.1 | <0.1 | <0.01 |
| 3-3 Effect of WO ₃ on aluminum capture | 0.01 | 0.3 | 0.6 | <0.01 | 0 |
| 3-4 Isotopic abundances | 0.5 | 0.5 | 0.5 | 0.5 | 0 |
| 3-5 Subtraction of captures due to contaminating isotopes ^c | 0.1 | 0.6 | 3.8 | 0.02 | 0 |
| 3-6 Statistical uncertainty in data points | 0.2-3 | 0.1-5 | 1-10 | 0.1-3 | 0.1-3 |
| 3-7 Boron flux shape | 1.0 | 1.0 | 1.0 | 1.0 | 1.0 |
| 3-8 Analyzer dead time correction | <0.01 | 0.01 | <0.01 | <0.01 | <0.01 |
| 3-9 Insensitivity to gamma spectrum changes | 0.1 | 0.1 | 0.1 | 0.1 | 0.1 |
| 3-10 Flux-capture flight path differences | <0.7 | <0.7 | <0.7 | <0.7 | <0.7 |
| 3-11 Background subtraction ^d | <0.3 | 1.3-5 | 2-11 | <0.2 | <0.3 |
| 3-12 Error in flux shape exponent ^e | <0.9 | <0.9 | <0.9 | <0.9 | <0.9 |

^a0 for W¹⁸².

^bThese limits might be exceeded in the 5- to 7.5-eV region in W¹⁸² and the 9- to 10-eV region in W¹⁸³, due to the large energy loss in oxygen scattering which might scatter neutrons into the low-energy resonances in these isotopes.

^cThese errors are exceeded in the peak region of the low-energy resonances.

^dErrors due to backgrounds are largest from 1 to 10 eV, and are very much smaller at other energies.

^e1 to 10 eV only.

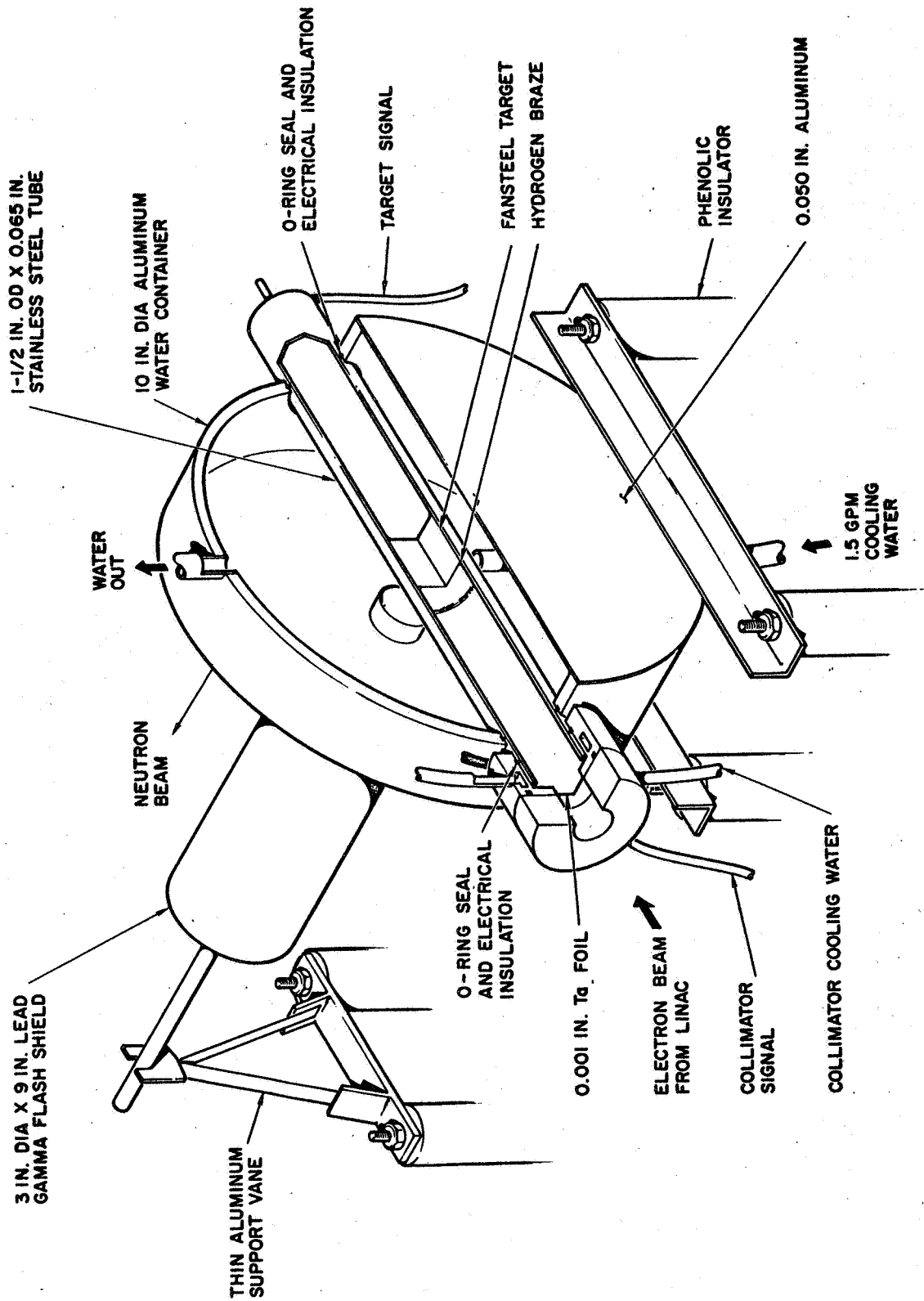


Fig. 1--Electron target and moderator assembly

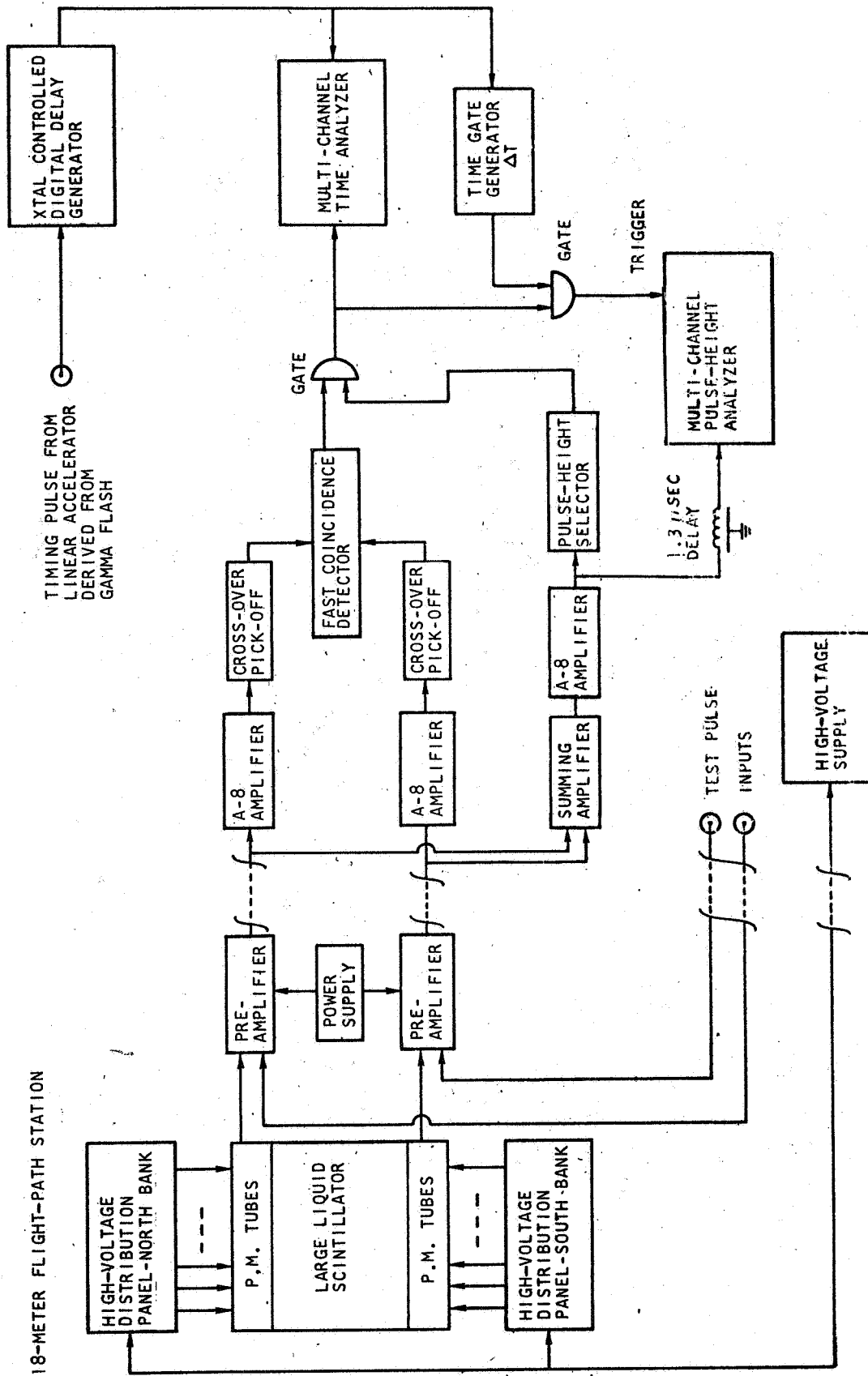


Fig. 2--Schematic of electronic configuration used in time-of-flight and pulse-height data acquisition

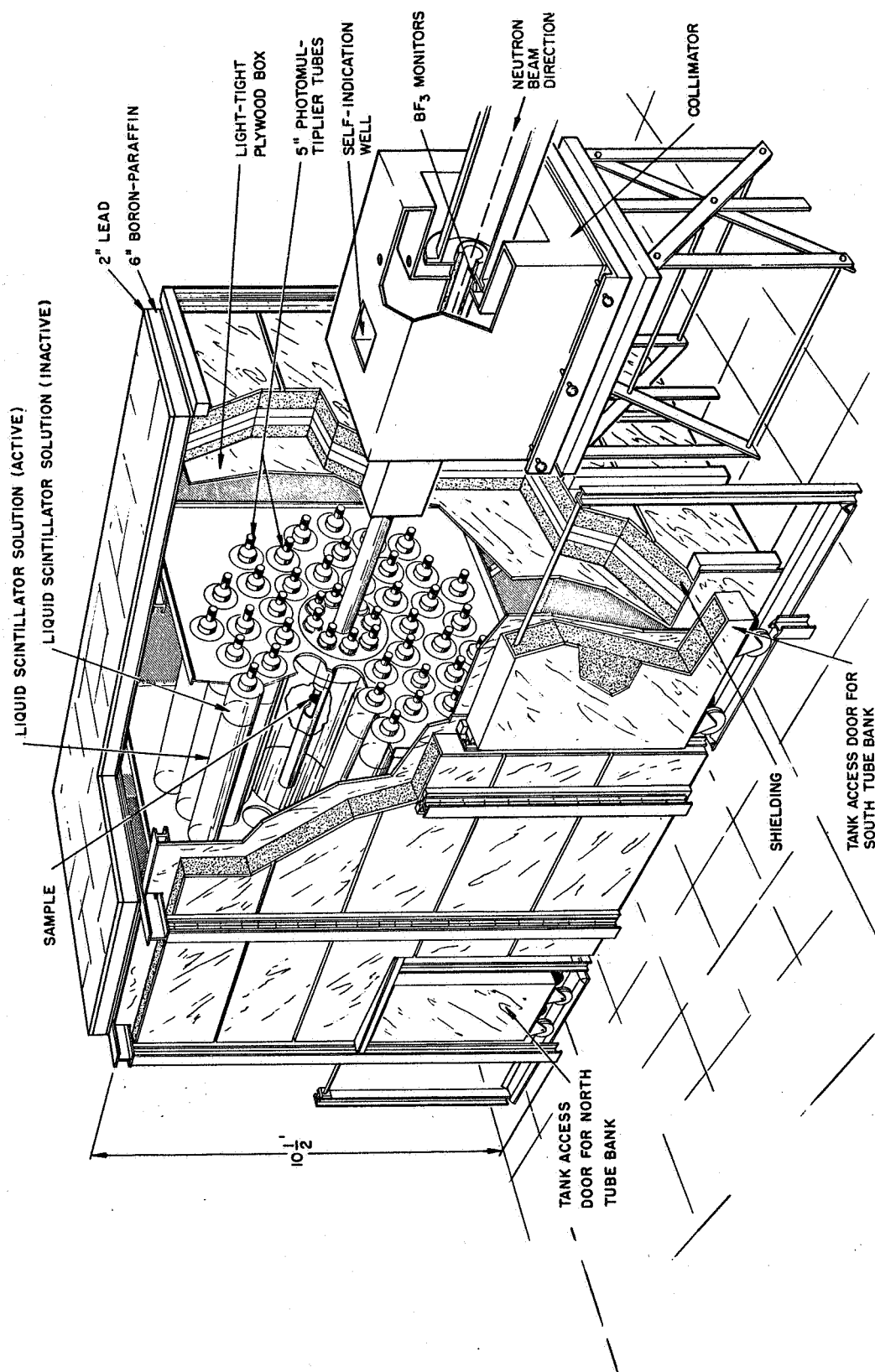


Fig. 3--View of large liquid scintillator showing the associated shielding and collimation

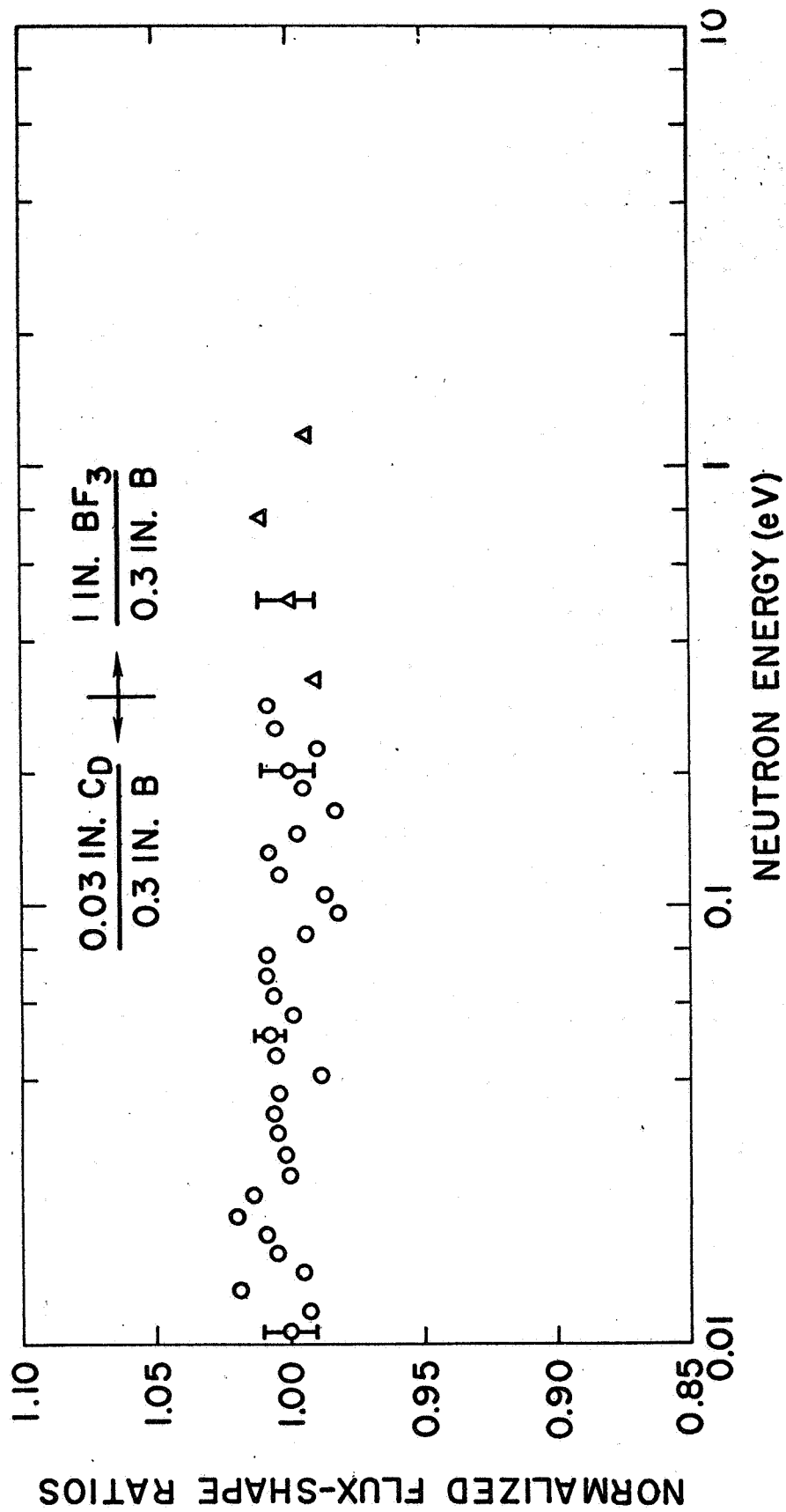


Fig. 4--Flux-shape comparisons using thick boron slab and cadmium samples and a thin BF₃ tube with a 1/v resonance

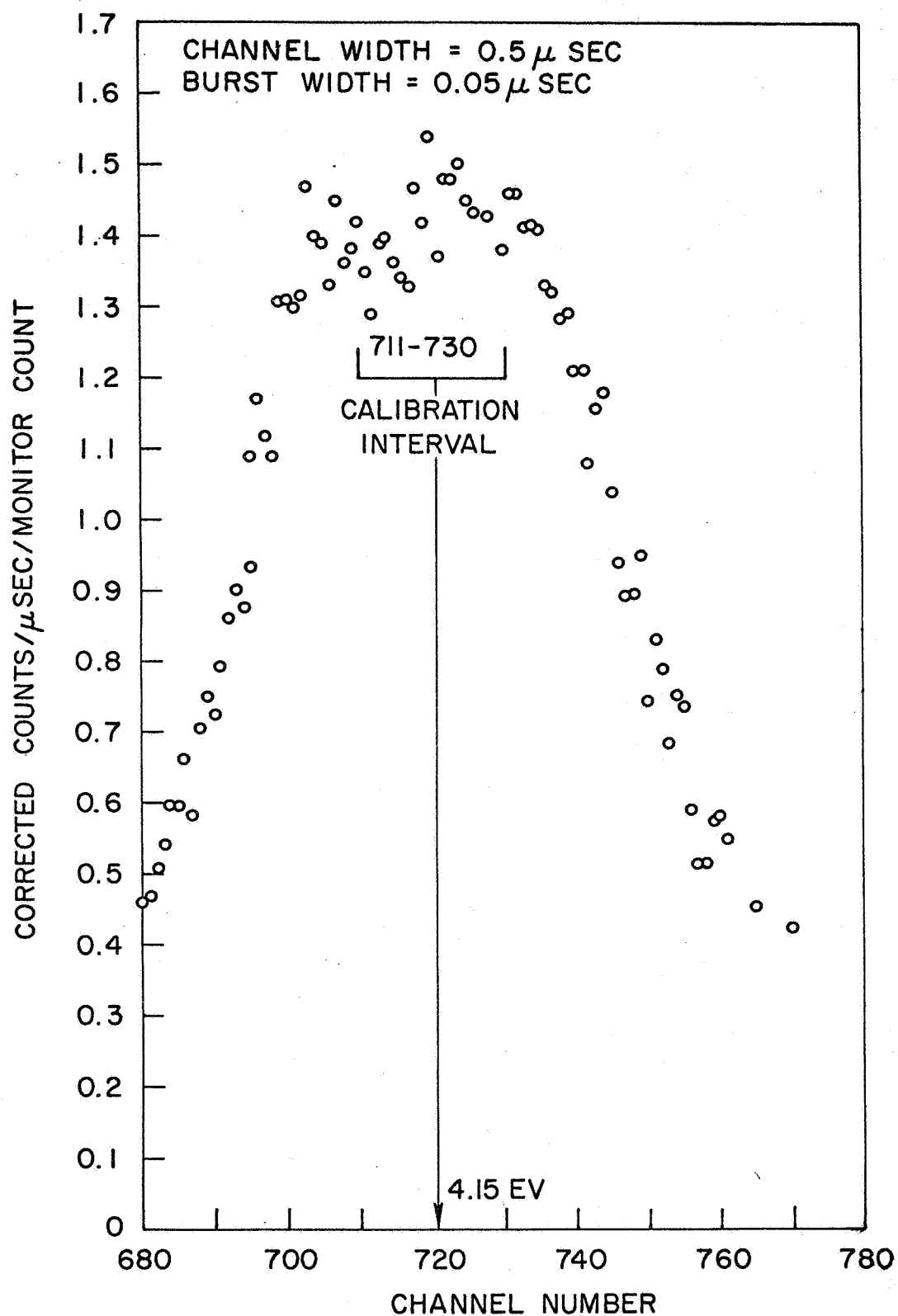


Fig. 5--Flux calibration data using the 4.15 eV resonance in W^{182} .
The sample is 0.01-in. natural tungsten.

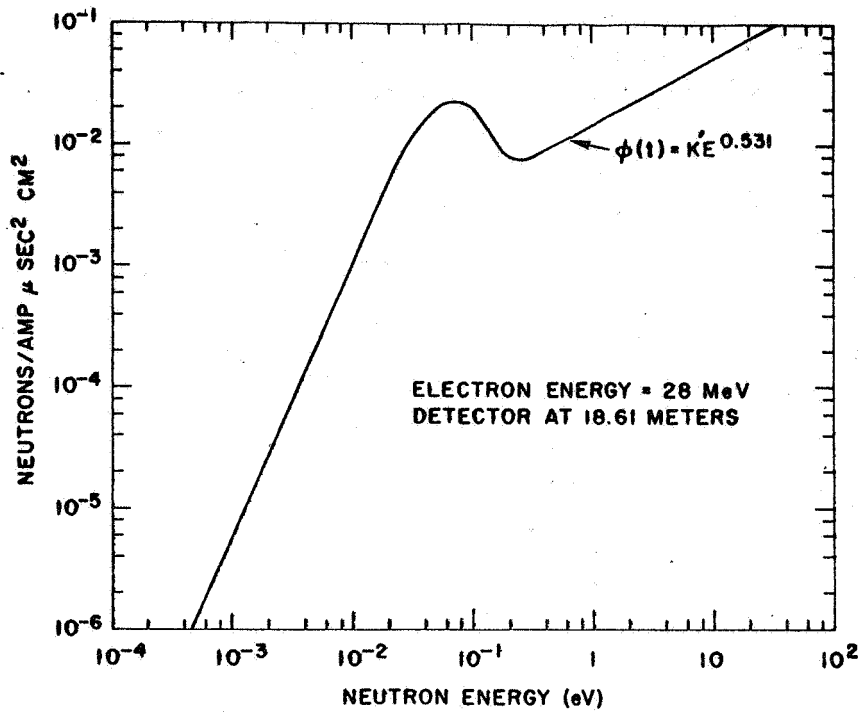


Fig. 6--Absolute neutron flux as a function of time

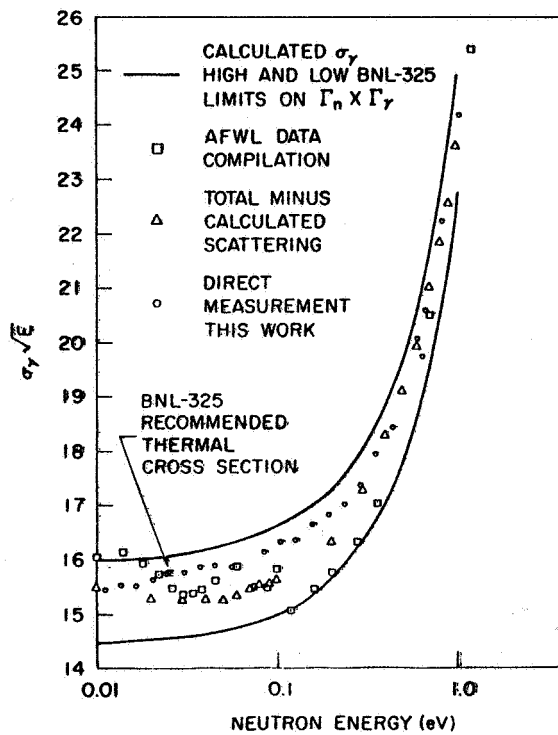


Fig. 7--Low-energy gold cross sections obtained from various sources

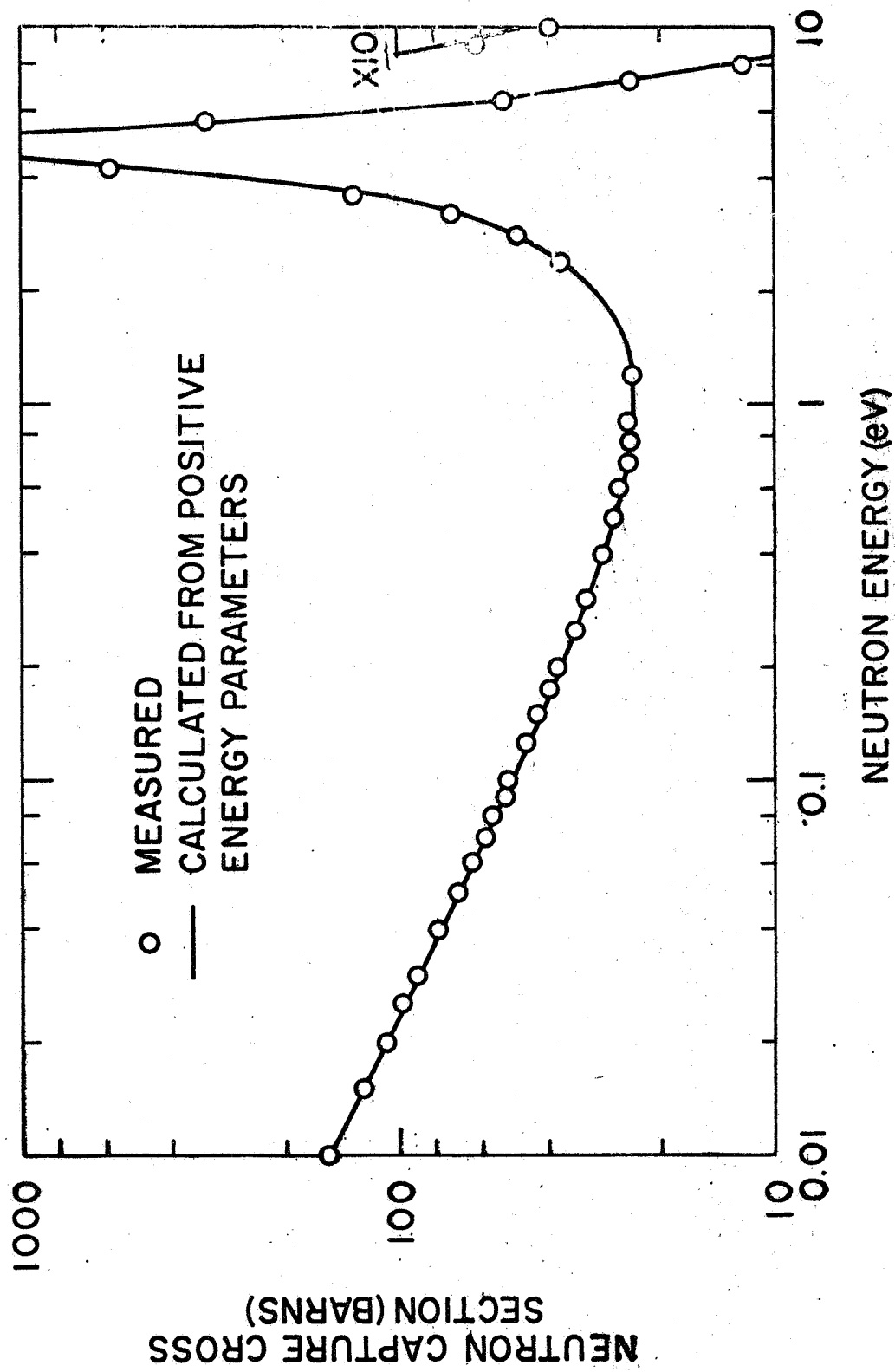


Fig. 8--Gold cross section

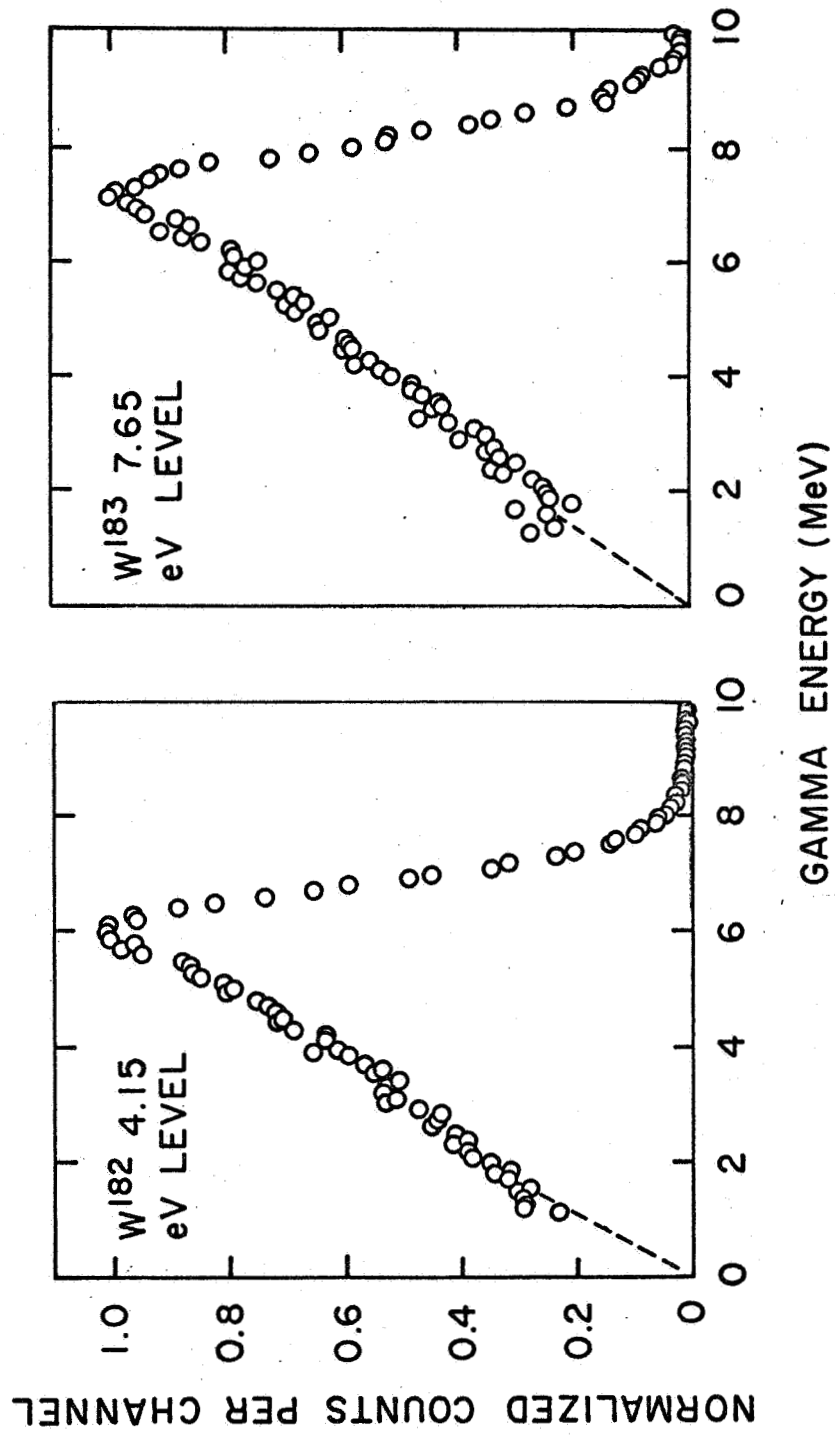


Fig. 9--Pulse-height distributions due to captures in W^{182} and W^{183}

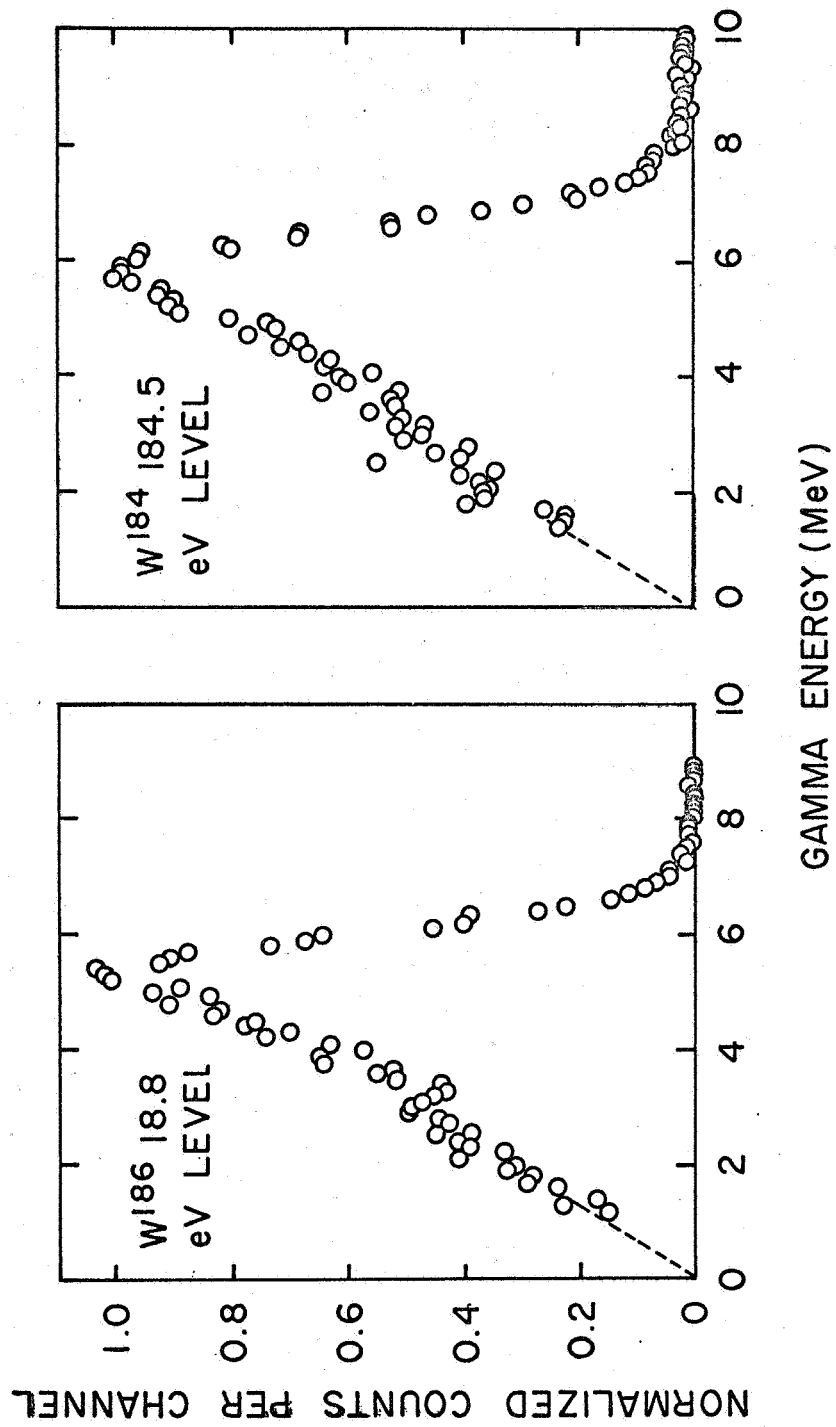


Fig. 10--Pulse-height distributions due to captures in W¹⁸⁴ and W¹⁸⁶

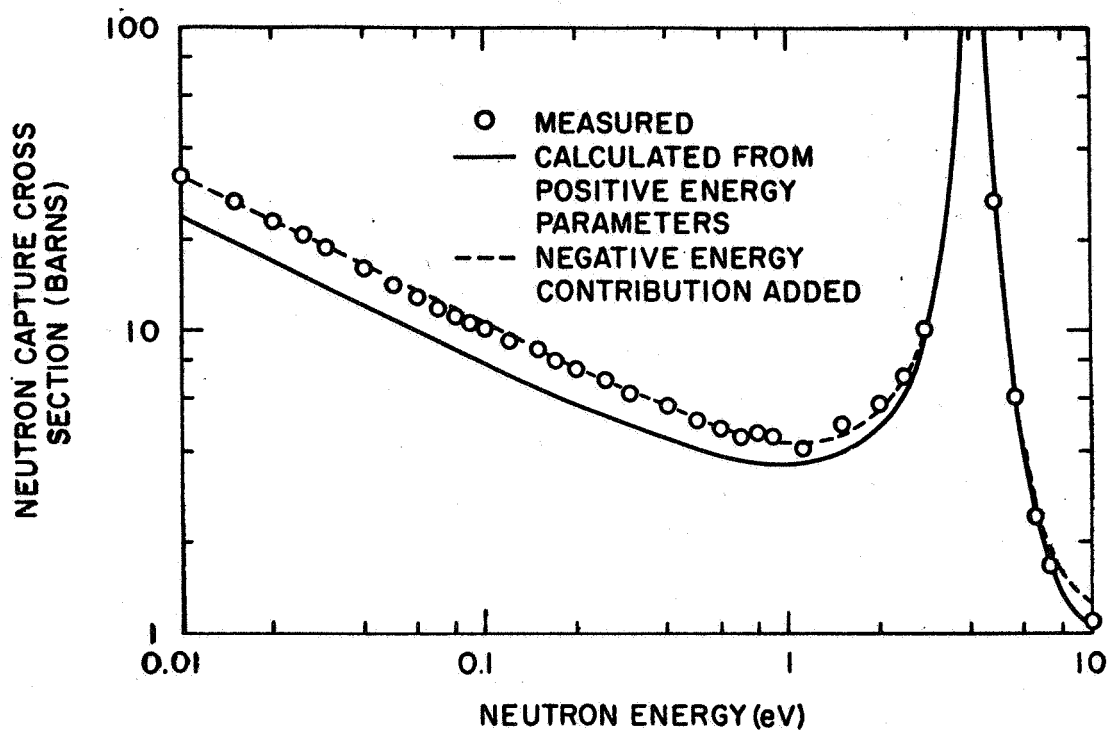


Fig. 11--Tungsten-182 cross section

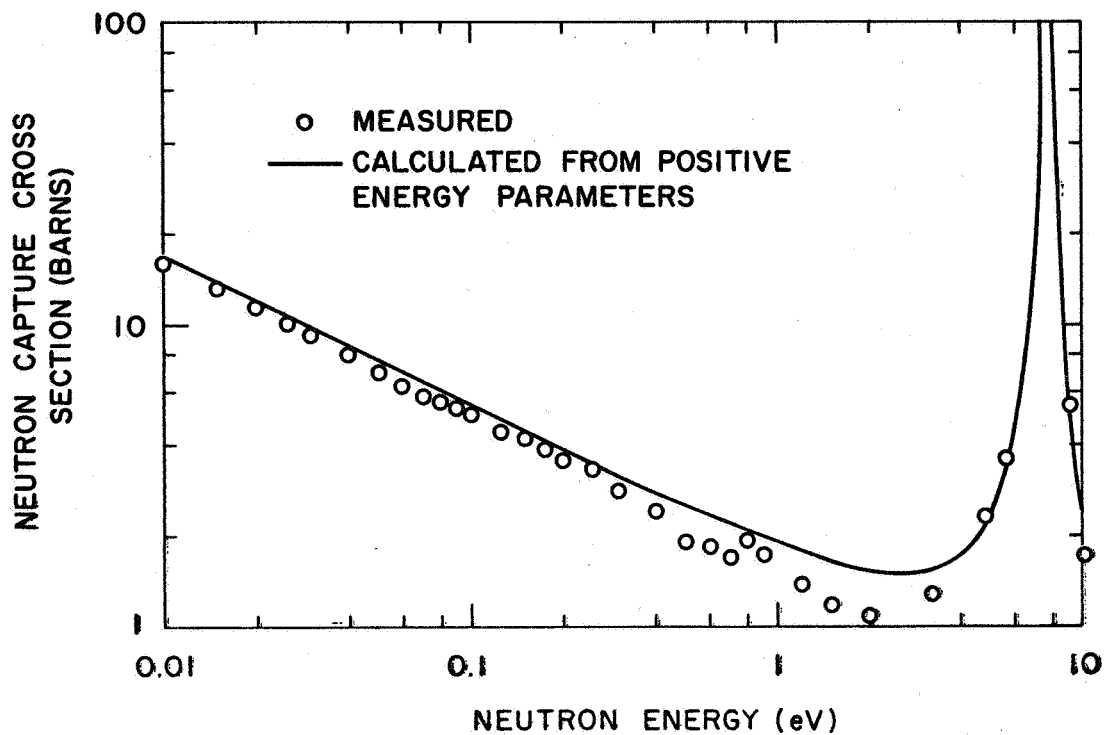


Fig. 12--Tungsten-183 cross section

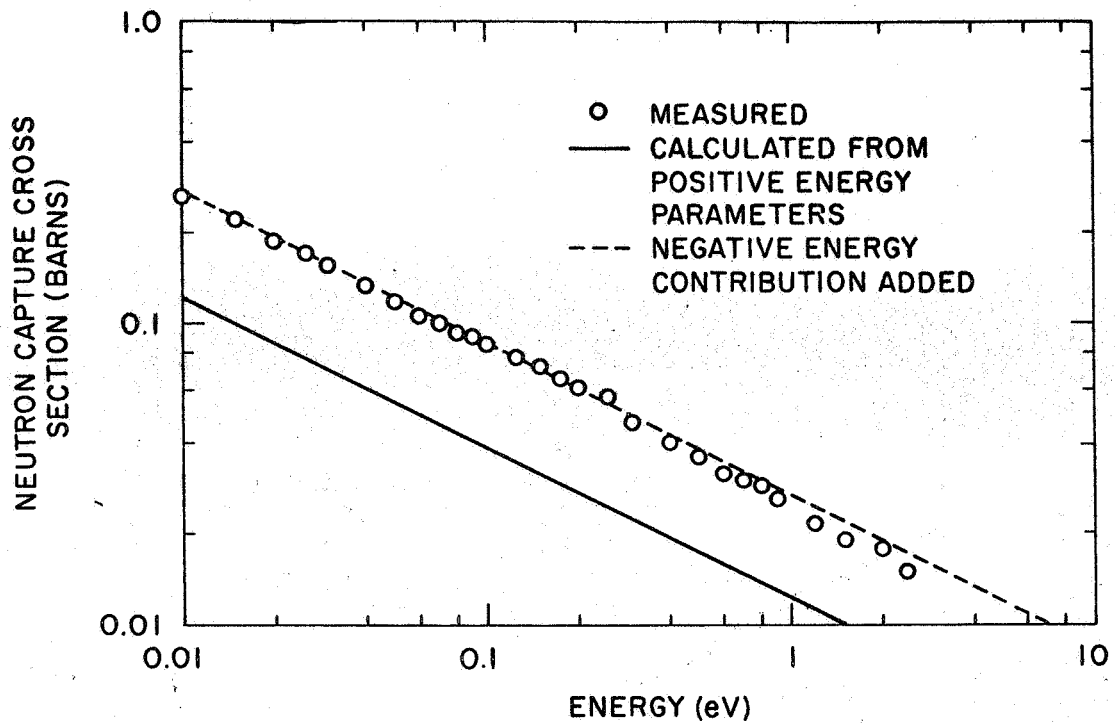


Fig. 13--Tungsten-184 cross section

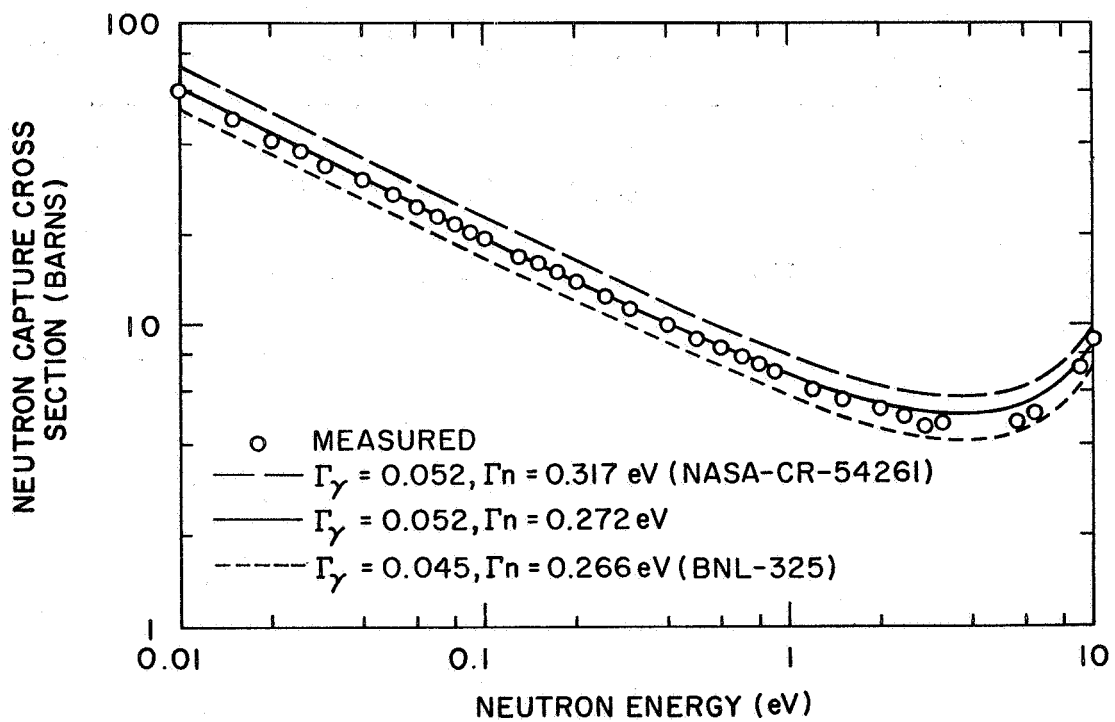


Fig. 14--Tungsten-186 cross section

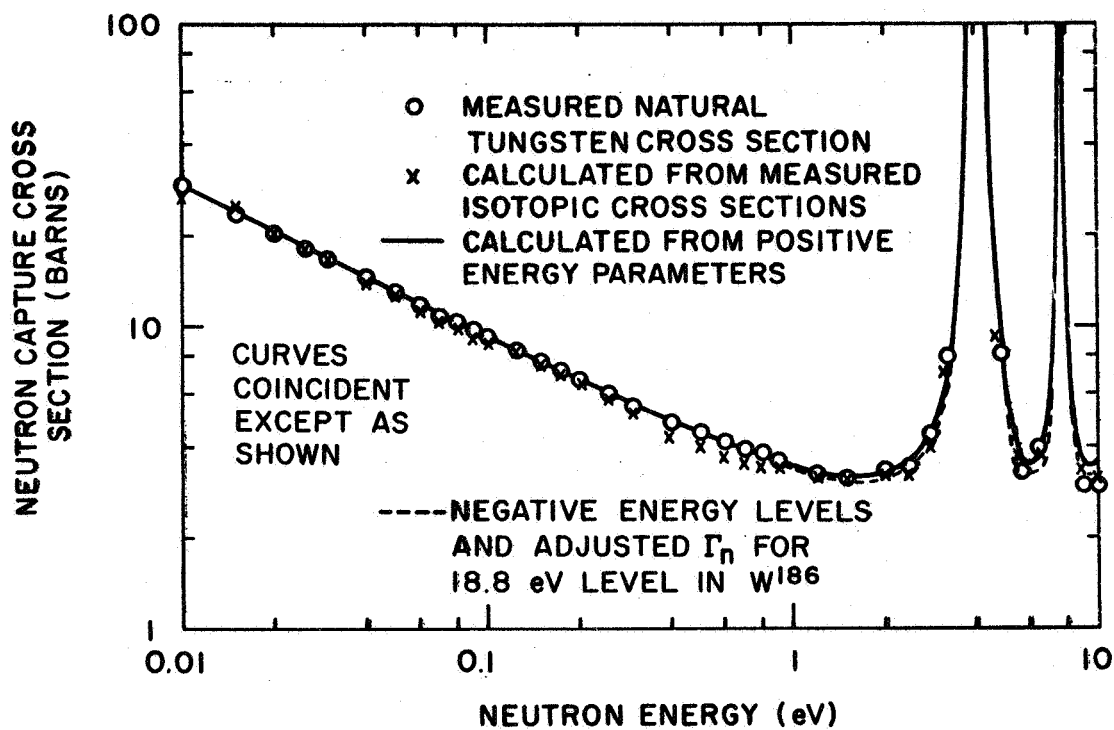


Fig. 15--Natural tungsten cross section